Research Article

Tracking morphologies at the nanoscale: Self-assembly of an amphiphilic designer peptide into a double helix superstructure

Karin Kornmueller[1], Ilse Letofsky-Papst[2], Kerstin Gradauer[1], Christian Mikl[1], Fernando Cacho-Nerin[3,†],
Mario Leypold[4], Walter Keller[5], Gerd Leitinger[6,7], Heinz Amenitsch[3], and Ruth Prassl[1] (✉)

[1] Institute of Biophysics, Medical University of Graz, BioTechMed-Graz, 8010 Graz, Austria
[2] Institute for Electron Microscopy and Nanoanalysis, Graz University of Technology and Graz Centre for Electron Microscopy, 8010 Graz, Austria
[3] Institute of Inorganic Chemistry, Graz University of Technology, 8010 Graz, Austria
[4] Institute of Organic Chemistry, Graz University of Technology, 8010 Graz, Austria
[5] Institute for Molecular Biosciences, Karl-Franzens-University Graz, 8010 Graz, Austria
[6] Research Unit Electron Microscopic Techniques, Institute of Cell Biology, Histology and Embryology, Medical University of Graz, 8010 Graz, Austria
[7] Center for Medical Research, Medical University of Graz, 8010 Graz, Austria
[†] Present address: Diamond Light Source, Harwell Science and Innovation Campus, Didcot OX11 0DE, United Kingdom

ABSTRACT

Hierarchical self-assembly is a fundamental principle in nature, which gives rise to astonishing supramolecular architectures that are an inspiration for the development of innovative materials in nanotechnology. Here, we present the unique structure of a cone-shaped amphiphilic designer peptide. While tracking its concentration-dependent morphologies, we observed elongated bilayered single tapes at the beginning of the assembly process, which further developed into novel double-helix-like superstructures at high concentrations. This architecture is characterized by a tight intertwisting of two individual helices, resulting in a periodic pitch size over their total lengths of several hundred nanometers. Solution X-ray scattering data revealed a marked 2-layered internal organization. All these characteristics remained unaltered for the investigated period of almost three months. In their collective morphology, the assemblies are integrated into a network with hydrogel characteristics. Such a peptide-based structure holds promise as a building block for next-generation nanostructured biomaterials.

Address correspondence to ruth.prassl@medunigraz.at

TSINGHUA UNIVERSITY PRESS ◯ Springer

1 Introduction

Nature offers elegant and efficient ways to create highly organized systems over several orders of magnitude by hierarchical self-assembly. This basic principle has been mimicked for the design of synthetic amphiphilic molecules in order to create novel materials [1–3]. Our study focused on short amphiphilic designer peptides. These molecules are exclusively composed of amino acids, and exhibit lengths of 4–10 amino acid residues. As their basic characteristic, they contain antagonistic hydrophilic and hydrophobic residues within the same molecule [4]. Self-assembling amphiphilic designer peptides have been explored as building blocks for the development of controllable, tailor-made, and biocompatible nanomaterials only recently. Because their structure is simple, yet variable, they have a huge scientific as well as economic potential. Their applications span the range from material sciences to chemistry and nanotechnology, and are of particular interest in nanomedicine due to the peptides' biocompatibility and biodegradability [5–7]. A constantly increasing global demand in innovative materials makes the elucidation of their assembly mechanism highly important.

A variety of supramolecular peptide-based architectures have been reported so far, including vesicles [8–10], spherical micelles [11–13], bilayered tapes [14, 15], donuts [16], helical and twisted ribbons [11, 12, 17, 18], fibers [12–14, 18, 19], rods [14, 19, 20], and tubes [8–11, 17, 21, 22]. Here, we report a new structural motif that can be added to the list of assemblies; for the first time a double-helix-like morphology was observed.

Only a few studies have investigated the elucidation of supramolecular peptide structures with scattering techniques [11, 17–19, 21], and none of the reported peptides have shown the propensity to form double helices. We used small angle X-ray scattering (SAXS), along with transmission electron microscopy (TEM), to investigate the different morphologies of nanostructures derived from varying concentrations of the amphiphilic designer peptide GAAVILRR. It is important to emphasize that these techniques operate in different length scales, and therefore give insights into different parts of the assembled nanostructures. SAXS allows monitoring of the self-assembly of biomolecules in solution, without the need of immobilization, labeling, or any other modification. It provides a detailed insight into the internal organization of structures in the low-nanometer range (~3–60 nm), and therefore can be used to describe the cross section of extended structures in high details. In contrast, longitudinal extensions, which often exceed the nanometer range, are well resolved with TEM. When combined, both techniques yield a detailed picture of the individual structure, as well as the collective morphologies in solution.

Our data indicates that the peptide concentration directly relates to the morphology, order, and complexity of the assembled structure. We monitored the transitions from monomeric systems to elongated single and double tapes, and finally to double-helix-like structures by increasing the peptide concentration.

2 Results and discussion

The newly designed amphiphilic peptide, GAAVILRR, is composed of eight amino acid residues. The hydrophilic head consists of two bulky, positively charged arginine residues, whereas the hydrophobic tail is composed of aliphatic amino acids with consecutively increasing hydrophobicity. The N-terminus is acetylated, keeping it uncharged. The C-terminus is amidated, resulting in an overall charge distribution of two positive net charges. The counterion is trifluoroacetate. Figure 1 illustrates the structure of a monomer. Lyophilized samples of varying concentrations were dissolved in water, resulting in optically clear, homogeneous, colorless solutions. These samples in highest concentration (75 mM) exhibited a gel-like appearance. In order to obtain fully developed structures, the samples were aged for 1 week. The molecule's amphiphilic nature endows a strong self-assembling ability in aqueous solutions above its critical aggregation concentration (CAC). For GAAVILRR, the CAC was estimated by fluorescence depolarization [23] to be about 30 mM in water (see Fig. S1 in Electronic Supplementary Material (ESM)).
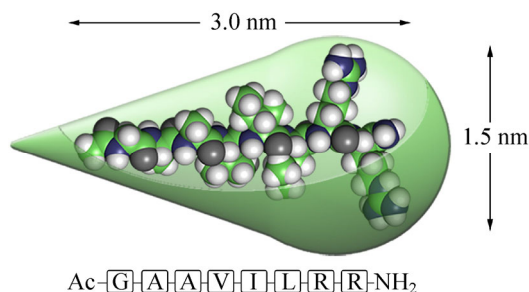
Figure 1 Molecular model of the amphiphilic designer-peptide, Ac-GAAVILRR-NH$_2$. The hydrophobic tail is composed of amino acids with consecutively increasing hydrophobicity and size. Two arginine residues provide the positively charged hydrophilic head. Peptide modifications include acetylation of the N-terminus and amidation of the C-terminus. The monomer length is approximately 3 nm, and its widest lateral extension is around 1.5 nm. The overall structure of the molecule looks like a cone. Color code: green: carbon, blue: nitrogen, gray: oxygen, and white: hydrogen.

Synchrotron SAXS was applied to investigate the self-assembly of GAAVILRR in solution as a function of peptide concentration. The individual scattering curves show concentration-dependent characteristics, and can broadly be divided into three groups (Fig. 2): low-concentration regime, intermediate-concentration regime, and high-concentration regime.

2.1 SAXS analysis of the low-concentration regime

First, we examined the peptide morphology at concentrations below or close to the CAC. This data could be modeled with the theoretical form factor of the peptide monomer, adding a hard-sphere interaction term [24]. The form factor was calculated with the program FoXS [25, 26], from a theoretical atomic model of the monomer (Fig. S2 in the ESM). Figure 2(a) shows the scattering curves of the peptide at concentrations ranging from 10 to 45 mM, with their respective fits (green curves) shown as a function of the scattering vector (q). All curves show the same characteristics with an almost linear region in the low q-range, followed by a broad shoulder at $q = 1.3$ nm^{-1}. The parameters to describe molecular interactions are obtained from the fitting function. As seen in Fig. 2(b), the hard-sphere radius (R_s) and the volume fraction (ϕ) remain constant for the measured concentrations. The averaged value of R_s, 1.6 nm, is in good agreement with the monomer's theoretical total length of 3 nm ($\approx 2R_s$). The linear increase in the

extrapolated intensity at zero angle (I_0) is directly related to the increasing peptide concentration, and is also visible in the constant value when I_0 is normalized to the concentration. Based on these characteristics we conclude that the transition from a dilute, noninteracting colloidal system (10 mM) to a more concentrated system (45 mM) occurs without supramolecular structure formation.

2.2 Structural heterogeneity dominates the intermediate-concentration regime

A pronounced change in the structure is observed when the peptide concentration is increased well above the CAC. Here, we distinguish between a transition structure (55–65 mM, Figs. 2(c) and 2(d)) and the final structure (75 mM, Figs. 2(e) and 2(f)). The SAXS pattern of the 55 mM sample shows a large increase in the intensity in the lower q-range, indicating the first steps of peptide assembly. At a slightly elevated concentration (60 mM), we observe a SAXS pattern typical of elongated structures. Increasing the concentration to 65 mM leads to a SAXS pattern that already shows distinct features of the endpoint structure, but does not show the high viscosity of the 75 mM sample.

SAXS measurements were complemented with TEM, which allows direct visualization of the assemblies. TEM pictures reveal a quite heterogeneous distribution of structures in the intermediate-concentration regime: Double-helix-like structures are the dominant species, along with extended tapes and double tapes (Fig. 2 (d$_1$–d$_3$)). Uniformity in tape width is observed by TEM throughout the intermediate morphologies.

2.3 Model development to fit the scattering curve of the highest peptide concentration

Increasing the peptide concentration to 75 mM results in a highly viscous solution, typical of hydrogels that are frequently reported in the context of amphiphilic peptides [12, 27]. Its scattering pattern, as shown in Fig. 2(e), exhibits four distinct features: a broad shoulder at $q \approx 0.1$–0.35 nm^{-1}, and three side maxima with consecutively decreasing intensities at $q = 0.5$, 1.18 and 2.4 nm^{-1}. In a first approach and for completeness, we tested various torus-like models to fit
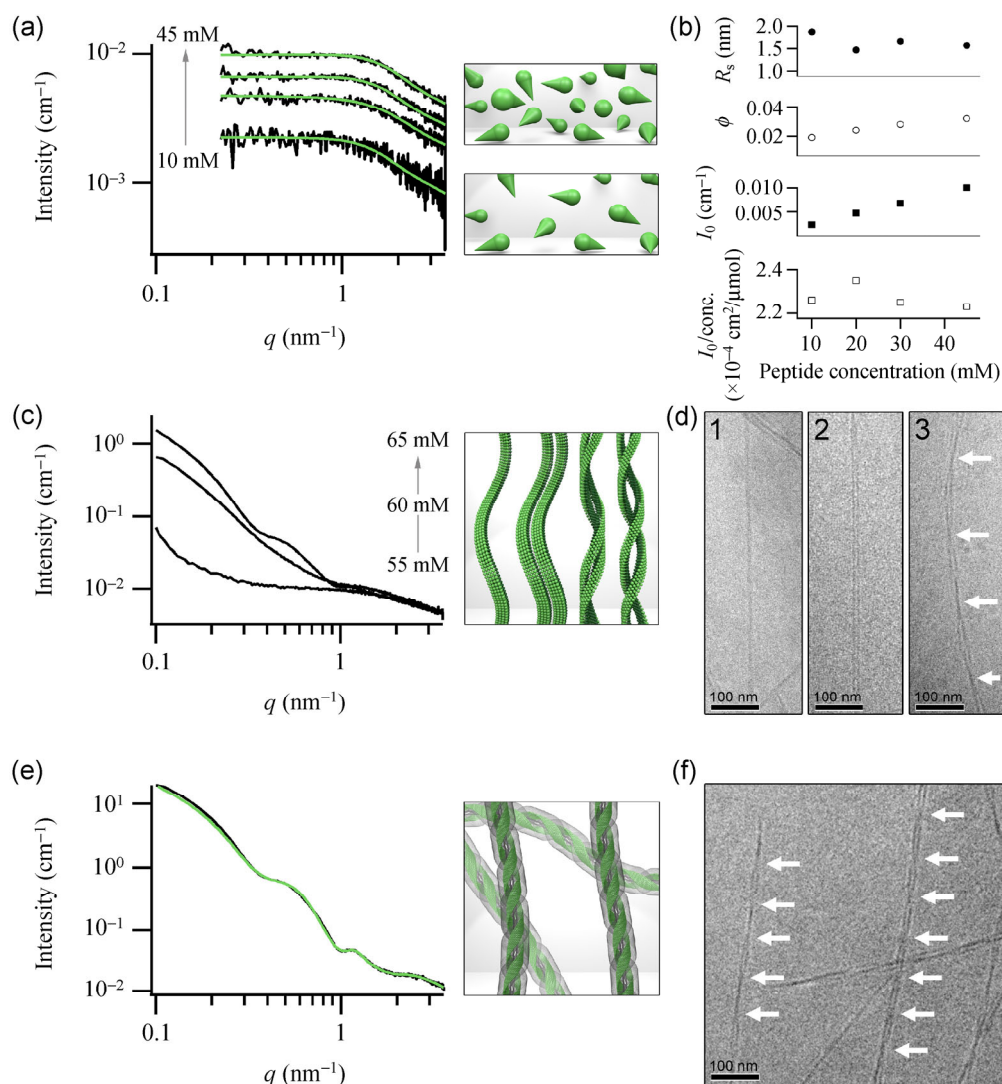
Figure 2 Concentration-dependent self-assembly of GAAVILRR. Scattering curves of GAAVILRR at different concentrations after 1 week of aging are shown with their respective fits. Schematic illustrations of the assembled structures and the corresponding Cryo-TEM images. (a) Low-concentration regime (10–45 mM). The fitting function that was used combines a hard-sphere model with the theoretical form factor of the peptide monomer; the fits are represented by the green curves. (b) Concentration-dependence of the fitted hard-sphere parameters, showing that the structures do not change over the investigated concentration regime. The hard-sphere radius (R_s) and volume fraction (ϕ) remain constant, whereas the extrapolated intensity at zero angle (I_0) increases linearly with concentration. Normalizing I_0 to the concentration results in a constant value. (c) Intermediate-concentration regime (55–65 mM). Several models obtained equally good fits (see Table S5 and Fig. S6 in ESM). This is in agreement with the observation of different intermediate structures using Cryo-TEM. (d) Selection of possible intermediates found at 60 mM. Both the single tapes (d_1) and parallel-aligned double tapes (d_2) are found. Double-helix-like structures are the dominant species (d_3), and are characterized by a periodicity between the intersection points. The double helices are several hundreds of nm in length, and 15–20 nm in width. All the intermediates have a related (single) tape width. (e) Hydrogel-forming sample (75 mM). The scattering curve was fitted with a double helix model combined with the theoretical form factor of the peptide monomer. (f) Cryo-TEM image of the double-helix-like structures at 75 mM. They are defined by using parameters identical to those of the assemblies in d_3, except for a slightly shorter distance of ~80 nm between the intersection points.

this curve, although TEM images suggested elongated structures. The rationale behind these tests was that Khoe et al. [16] investigated a peptide with a similar sequence, lacking just one alanine residue, which formed donut-like structures in solution. However, our scattering curve cannot be properly described by a torus, a torus with an elliptical cross section, shell-models thereof [28], or elongated stacked tori (for a description of the fitting functions and the respective fits, see Fig. S3 and Table S1 in ESM). Also, a twisted ribbon model [29, 30] can be excluded due to its imperfect fit (see Fig. S4 and Table S2 in ESM). Application of a helical fitting function greatly improves the fit (Fig. S5 and Table S3 in ESM). However, it is only after extending the helical model [30] to a layered double helix, based on the equations of Pringle et al. [31], that the fitting results can be obtained with a minimal chi-square value [32]. In our study, a double helix is defined as two single helices that fit into each other, and are displaced by angle φ. This formalism introduces a coupling of the different layer lines, which is typical of the helical diffraction pattern [33]. The amplitudes of the single layer lines given by the values of tape width and φ discriminate between single and double helices. Equally good fits are achieved by using single and double helix models for the intermediate structures from 55 to 65 mM (for details, Table S5 and Fig. S6 in ESM). As stated above, this concentration regime represents an intermediate state of a dynamic structure evolution process, where the coexistence of different morphologies is seen. Both the single helical tapes and double-helix-like structures are present. Even the existence of twisted ribbons, often described as precursors in helix formation, cannot be excluded. This heterogeneity is represented by the imperfect fit of any single model to the SAXS data at intermediate concentrations. Ensemble analysis shows a distribution of approximately 65% single helices and 35% double helices (Fig. S7 and Table S6 in ESM). The situation is different for the highest peptide concentration; in this region, the population of structures is more homogenous. The assemblies can be best described as two individual ribbons that are tightly intertwined (i.e., not loosely connected), showing highly regular repeat distances at their intersection points (Fig. 2(f)). Because of this regularity

and homogeneity in their total widths, an interaction between the two strands seems likely. Therefore, we describe them as double-helix-like structures, and indeed, fitting with the developed 2-layered double helix model results in an excellent fit to the experimentally obtained scattering data.

### 2.4 SAXS-derived double helical model

The X-ray derived parameters describing the novel 2-layered double helical model are illustrated in Fig. 3 (see also Table S4 in ESM). The double helix exhibits a pitch (P) of ~60 nm and a mean radius (R) of 6 nm, resulting in a helical twist angle of $\alpha \sim 60°$. The tape height along the longitudinal axis (w_h) is ~23 nm (Fig. 3(a)). The diameter of the double helix is ~16 nm (Fig. 3(b)), indicating that no change in the overall width of the tape has occurred upon hydrogel formation. Most importantly, the electron density profile (ρ) derived from the SAXS data allows for a sectioning of the tape into several layers (Fig. 3(c)). Accordingly, the peptide-containing region accounts for ~3.5 nm of one tape. The inner hydrophobic core has the highest electron density and spans approximately 1 nm (D_1). In this innermost region, we expect antiparallel stacking of the peptide monomers due to intermolecular hydrogen bonding. Given a monomer length of ~3 nm, we assume a very tight packing and interdigitation of the two monomers, and we suggest that this organization determines the high stability of the supramolecular structures. Figure 3(d) shows one sterically permitted arrangement for the stacking of a peptide pair, and the respective hydrogen bond distribution. The hydrophobic core region is flanked by a region providing the space for the hydrophilic head groups. A decrease in the electron density, from $\rho_1 = 1.4$ to $\rho_2 = 0.8$ electrons/Å^3, points to a less densely packed zone, which indicates a higher flexibility of the head groups. In addition, the electron density distribution map shows an area that is characterized by a diffuse scattering contribution (ρ_3). We attribute this region to a low fraction of twisted ribbons (below 5%) that coexist in the sample. They are characterized by the same tape width (12 nm) as those forming the double-helix-like structures. The structural morphology of the highest peptide concentration was also approached by three different

TEM techniques: freeze-fracture, negative-staining, and Cryo-TEM. All three techniques support our model of two individual tapes that intertwine to form the double-helix-like structures. The images, as well as a discussion on the strengths and limitations of either technique, can be found (Fig. S10 in the ESM).

2.5 Spectroscopic techniques to monitor the structure's internal organization

To obtain additional information about the internal organization of the structures and to confirm our model of antiparallel organized monomers (as proposed in Fig. 3(d)), we applied circular dichroism (CD) and attenuated total reflection Fourier transform infrared (ATR-FTIR) spectroscopy. In principle, the obtained CD spectra demonstrate a transition from mainly random-coil (1–45 mM, Fig. 4(a)) to predominantly β-type structures (60 mM, Fig. 4(b)). The lowest peptide concentrations show a large negative p→p* transition at 198–202 nm, followed by a negative
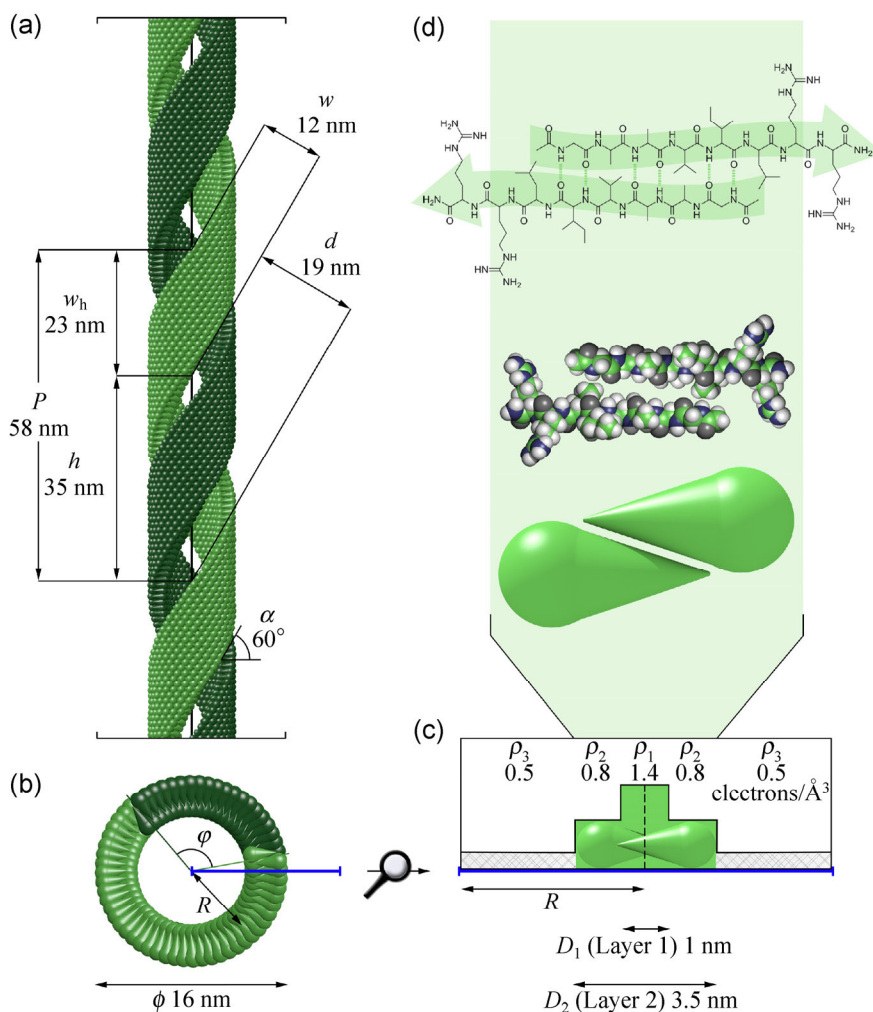
Figure 3 Structural parameters of the double helical model. Values are based on the 75 mM sample fit presented in Fig. 2(e). (a) Side-view of the double helix composed of GAAVILRR molecules. Two individual strands are intertwisted to form a double-helix-like structure. The illustrated parameters are the pitch (P), helical twist angle (α), tape thickness (w), tape height (w_h), free space between one tape (h), and corresponding free space in the bilayer plane (d). (b) The cross section shows the mean radius (R) and angle (φ) by which the two tapes are displaced with respect to each other. (c) Electron density distribution of the cross section, which can be divided into individual shells, with D_1 and D_2 being the shell distances with electron densities, ρ_1 and ρ_2. Electron density ρ_3 (gray mesh) reflects the contribution of a low fraction of twisted ribbons in the sample. The dashed line represents the symmetry line. In the innermost region (highlighted in green), we expect hydrogen bonding between antiparallel aligned peptide molecules. (d) The hypothesized arrangement of two peptide molecules, together with a proposed hydrogen bond distribution pattern depicted in the chemical formulas. Color code of the molecular model of GAAVILRR: green: carbon, blue: nitrogen, gray: oxygen, and white: hydrogen.

(a)

1–45 mM

(b)

60 mM

(c)
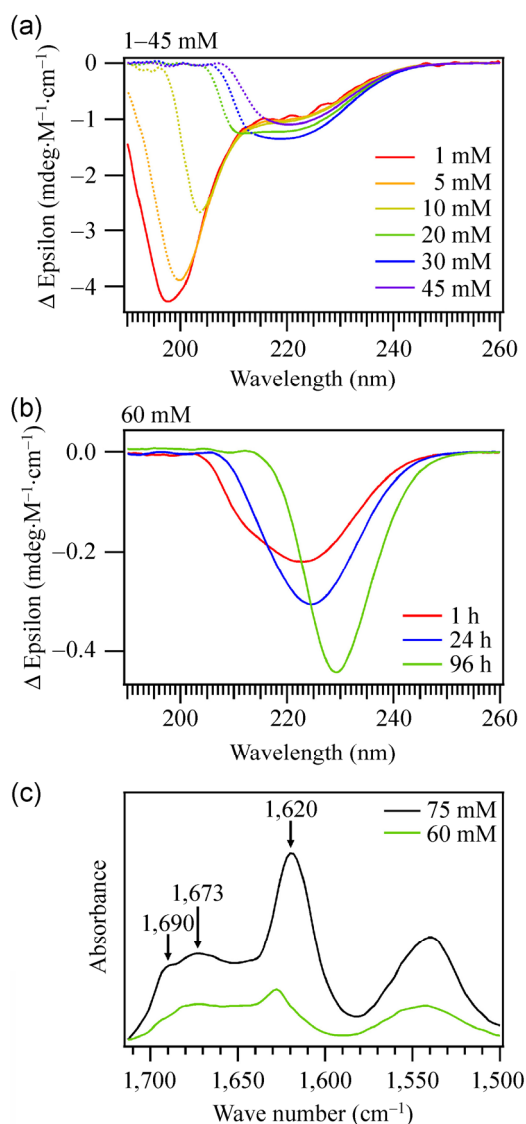
Figure 4 Transition from random-coil (1–45 mM) to β-type structures (60–75 mM), measured by circular dichroism and infrared spectroscopy. (a) CD spectra of the low-concentration samples recorded after 10 days of incubation. (b) CD spectra of the 60 mM sample recorded at different time points over an incubation time of 4 days. Dotted lines represent parts of the spectra where a threshold of 600 V in the high-tension (HT) signal was exceeded. (c) ATR-FTIR spectroscopy confirms the presence of antiparallel β-sheets (peaks at 1,620 and 1,690 cm^{-1}), the peak at 1,673 nm^{-1} is indicative of residual TFA.

band with a maximum at 220 nm, which can be assigned to the n→p* transition. These characteristics are associated with a mainly random-coil structure. The large negative peak becomes less pronounced with increasing peptide concentration, and is shifted to higher wavelengths. This change is consistent with

a rapid increase in the high-tension (HT) voltage, and therefore, these parts of the spectra (dotted lines) should be considered with caution.

Nevertheless, all spectra of the low-concentration regime point to a random-coil structure. In the 60 mM sample, the β-strand content significantly increases, and the spectroscopic characteristics develop towards a negative maximum at 230 nm (Fig. 4(b)). Although very few reports exist on how to interpret this large negative peak at 230 nm, there is a consensus that it is related to β-type structures [18, 34, 35]. A red shift in the signal has been associated with a higher degree of twisting in β-sheets than that of planar β-sheets [27]. CD spectra with striking similarity to ours were reported in the literature [36, 37]; interestingly, all these spectra were related to double helices. We now hypothesize that a CD spectrum like ours—characterized by the absence of the typical positive peak at 190–200 nm, and a single large negative band around 230 nm—could be directly associated with the double helix morphology formed when β-strands are present.

ATR-FTIR measurements confirmed the presence of β-sheet structures (Fig. 4(c)). The major amide I peak at 1,620 nm^{-1} is characteristic of β-sheet interactions. The weak band at 1,690 nm^{-1} can be assigned to an antiparallel component, whereas the contribution at 1,673 nm^{-1} arises from residual trifluoroacetic acid (TFA) in the sample. In comparison, both the 60 mM and 75 mM samples show the same spectroscopic characteristics, as well as the typical scaling of the signal with concentration.

The results of CD and ATR-FTIR spectroscopy are consistent with our proposed model of tightly packed, interdigitated peptide molecules that are held together by hydrogen bonding due to antiparallel stacking.

2.6 Evolution of structure over time

To determine whether the double-helix-like structures are intermediates that develop for the often-described tubular structures, or whether they are a final state of the assembly, we performed a series of SAXS and Cryo-TEM measurements at different time points over 11 weeks. The SAXS pattern of the 75 mM sample remains unchanged over the observed

period (1, 4, and 11 weeks), revealing that the overall structure and the internal organization do not change (see Fig. S8 in the ESM). These results are further supported by Cryo-TEM micrographs, in which stable double-helix-like structures are observed at every time point (Fig. 5). Only 30 min after dissolution, a double-helix-like morphology develops and shows the final widths of ~15–20 nm, and a mean distance between periodic intersection points of ~80 nm (see white arrows in Fig. 5). These characteristics remain unaltered for at least 11 weeks.

An interesting point that needs to be addressed is the strikingly different morphology of GAAVILRR compared to the structure of the peptide GAVILRR reported by Khoe et al. [16], which differs from our sequence in lacking just one alanine residue. While GAVILRR forms donut-like structures in solution, we have found double-helix-like assemblies for GAAVILRR. These results highlight the fact that minor differences in the amino acid composition can have a huge influence on the resulting structures. In fact, this feature is not unique, and systematic variations of the tail length or the substitution of

single amino acids in a given sequence are a matter of intense research [12, 13, 18, 27, 38, 39]. A deeper understanding of the role of every single amino acid opens up the opportunity for tunable structures. They are highly desirable for the multifaceted application fields of supramolecular self-assembled nano-structures. Whether the double helical arrangement of amphiphilic designer peptides has previously been overlooked due to experimental limitations, or is a unique novel feature related to peptide sequence remains unresolved.

3   Conclusions

We have shown that the structure of supramolecular peptide assemblies in solution strongly depends on the peptide concentration. Below the CAC, the peptides are dispersed as monomers and do not display superstructural features. According to Cenker et al. [40], as soon as lyophilized peptides are dispersed in water above their CAC, one part of the molecules is present in the form of aggregates, whereas the other part (equal to the concentration of the CAC) is in its molecularly dissolved state. In a time-dependent crystal growth process, the aggregates grow by uniaxial extension through the assembly of monomers. In a dissolution-reassembly mechanism, structures with a high level of perfection are grown within minutes to a few hours. At this stage, the structures already exhibit a definite cross section with their equilibrium diameters [40]. We observed bilayered tapes, in which we expect that hydrophilic arginine residues exposed to the solvent and the hydrophobic tail residues interdigitated and tightly packed in the interior were stabilized by intermolecular hydrogen bonding. Because of the peptides' intrinsic chirality, the monomers do not assemble in a strictly parallel manner, but slightly tilt with each other, leading to twisted structures. In addition, a nonplanar alignment of the monomers leads to bending. This accounts for a twisted-to-helical transition on the one hand, and on the other hand limits the lateral growth, thus favoring uniaxial elongation [29, 41, 42]. Hence, double-helix-like structures, with several hundred nanometers to micrometers in length but only around 16 nm in width, can develop. Because of the high
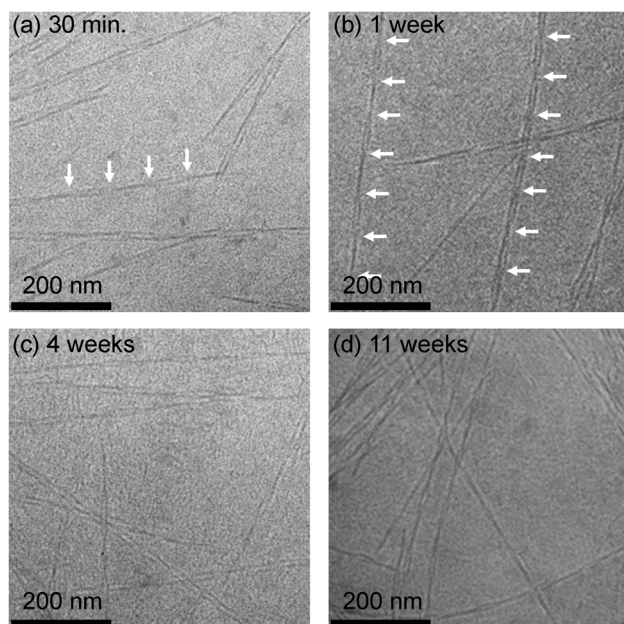
Figure 5   Cryo-TEM of 75 mM GAAVILRR at different time points, (a) freshly dissolved, (b) 1 week, (c) 4 weeks, and (d) 11 weeks, show no alteration in the global morphology. The peptide forms double helices at every time point, with similar structural parameters: width ~15–20 nm and intersection points every ~80 nm (see white arrows).

regularity of pitch distances, the orientation of the two individual strands seems to be the consequence of a sensitive interplay between geometrical constraints, intertape hydrogen bonding interactions, hydrophobic affinity of the tail residues, and electrostatic repulsion of the positively charged arginine residues. Finally, the double-helix-like superstructures assemble into a network displaying gel-like features. As these intertwined assemblies are stable for several months, this architecture seems energetically and sterically highly favorable. Keeping in mind the manifold applications for supramolecular self-assembled structures [4, 5, 43–47], a double-helix-like tape might be the building block for the next-generation bioinspired nanomaterials.

4 Methods

4.1 Peptide preparation

Ac-GAAVILRR-NH$_2$ was custom synthesized and purified by piCHEM GmbH (Graz, Austria) following the general procedure for Fmoc solid-phase peptide synthesis. The samples were prepared by dissolving the lyophilized peptide in double distilled water to obtain the desired concentrations. The samples were incubated at 4 °C under an argon atmosphere for 1 week prior to SAXS and TEM measurements.

4.2 Small angle X-Ray scattering (SAXS)

Synchrotron X-ray scattering data was collected at the Austrian SAXS beamline at ELETTRA (Trieste, Italy) [48]. The measurements were carried out at a wavelength of 0.154 nm and a sample-detector distance of 1.1 m. The photon energy was 8 keV. The data were recorded with a Pilatus detector (PILATUS 100 K, DECTRIS Ltd., Villigen PSI, Switzerland), calibrated with silver behenate. The scattering intensity was measured as a function of the scattering vector (q),

$$q = 4\pi \, (\sin\vartheta)/\lambda,$$

where 2ϑ is the scattering angle and λ is the wavelength. The samples were measured either in a 1.5 mm glass capillary (10–60 mM) or in a gel sample holder (75 mM). A discussion on the influence of shearing forces when filling the capillary can be found in Table S7 and Fig. S8 in the ESM. Data analysis was performed using Fit2D [49] and Igor Pro (Version 6.22A, WaveMetrics Inc., USA). Experimental intensities were normalized to sample transmission and corrected for background. Absolute calibration was performed using water as the secondary standard, using the method described by Orthaber [50].

4.3 Formal description of a helix and a double helix: fitting parameters

The mean radius (R) is the distance between the helix center to the center of the innermost shell. The cross section of our model comprises two to three layers with their respective distances (D_1–D_3) and electron densities (ρ_1–ρ_3). Parameter ρ_{solvent} is the electron density of the solvent, which was maintained constant at 0.335 e/Å^3. The mean radius and pitch (P) provide the helical twist angle α, where $\alpha = \arctan[P/(2\pi R)]$. It describes the angle of the helix with respect to the equatorial plane. The rotation angle (ω) reflects the degree of opening of the helix. The thickness of the tape (w) is defined as $w = \omega D3 \sin\alpha$, the tape height (w_h) is defined as $w_h = w/\cos\alpha$, and the free space between the tapes (h) is defined as $h = P - w_h$. The free distance (d) between the tapes in the bilayer plane is defined as $d = (wh)/w_h$ [30, 51].

A double helix results from two single helical tapes (with the same properties as described above) that are displaced with respect to each other by angle φ. The pitch of a single helix should be greater than the tape height (w_h) in order to leave room for the second tape.

4.4 Cryogenic transmission electron microscopy (Cryo-TEM)

The samples were adsorbed onto a glow-discharged carbon-coated copper grid, blotted to create a thin film, plunged into liquid ethane, and transferred to liquid nitrogen. Vitrified specimens were transferred onto a Gatan 626-DH cryo transfer specimen holder and imaged at cryogenic temperatures in a Tecnai T12 (FEI, The Netherlands) microscope, operated at 120 kV.

4.5 Circular dichroism (CD) spectroscopy

Measurements were conducted on a JASCO J-715 circular dichroism spectrometer (Jasco Inc., Easton,

MD) using a 0.1 mm path length cell. The spectra were recorded between 185 and 260 nm in the interval scan mode with 0.2 nm resolution and an average time of 1 s. The scan speed was 50 nm/min. Spectra of the low-concentration samples (10–45 mM) were recorded after 10 days of incubation. The 60 mM sample was filled into the capillary directly after dissolution, and its structure evolution was monitored over 4 days. Because of the high viscosity of the 75 mM sample, it was not possible to fill the sample into a measurement cell. The final spectra were corrected for background by subtracting the corresponding buffer spectra obtained under identical conditions. Data processing and analysis were performed with CDtool [52] and Igor Pro (Version 6.22A, WaveMetrics Inc., USA). The threshold of the high-tension (HT) voltage signal was set to 600 V. Parts of the CD spectra exceeding this threshold are marked by dotted lines.

4.6 Attenuated total reflection Fourier transform infrared (ATR-FTIR) spectroscopy

Infrared spectra were recorded between 4,000 and 600 cm^{-1} on a Bruker TENSOR 37 FTIR spectrometer, equipped with an ATR accessory (Bruker Optics Inc., Billerica, USA). The spectra were the averages of 128 scans with a resolution of 4 cm^{-1}. Data analysis was performed with the OPUS software (Version 6.5, Bruker Optics Inc., Billerica, USA).

4.7 Artwork

Illustrations of the assembled structures were created with Blender (Version 2.66, Blender Foundation) [53] and Adobe Photoshop CS5 Extended (Version 12.0.3 × 32, Adobe Systems Inc., USA). Chemical formulas were drawn with ChemDraw (Version 6.0.1, Perkin Elmer Informatics, USA).

Acknowledgements

Electronic Supplementary Material: Supplementary material (experimental details; determination of the CAC; SAXS; fitting functions: hard-sphere model, theoretical form factor of a peptide monomer, torus, torus with elliptical cross section, core-shell model of a torus and a torus with elliptical cross section, stacked models thereof, helix, double helix; fits and derived parameters of the torus-, twisted ribbon- and helix-models; ensemble analysis for coexisting structures, time evolution of the 75 mM sample. The influence of shearing forces on the resulting SAXS pattern when filling the capillary. Comparison of freeze-fracture, negative-staining and Cryo-TEM techniques for the direct visualization of superstructures) is available in the online version of this article at http://dx.doi.org/10.1007/s12274-014-0683-9.

References

[1] Luo, Z. L.; Zhang, S. G. Designer nanomaterials using chiral self-assembling peptide systems and their emerging benefit for society. *Chem. Soc. Rev.* **2012**, *41*, 4736–4754.

[2] Zelzer, M.; Ulijn, R. V. Next-generation peptide nanomaterials: Molecular networks, interfaces and supramolecular functionality. *Chem. Soc. Rev.* **2010**, *39*, 3351–3357.

[3] Aida, T.; Meijer, E. W.; Stupp, S. I. Functional supramolecular polymers. *Science* **2012**, *335*, 813–817.

[4] Zhao, X. B.; Pan, F.; Xu, H.; Yaseen, M.; Shan, H. H.; Hauser, C. A.; Zhang, S. G.; Lu, J. R. Molecular self-assembly and applications of designer peptide amphiphiles. *Chem. Soc. Rev.* **2010**, *39*, 3480–3498.

[5] Ellis-Behnke, R. G.; Liang, Y.-X.; You, S.-W.; Tay, D. K.; Zhang, S. G.; So, K.-F.; Schneider, G. E. Nano neuro knitting: Peptide nanofiber scaffold for brain repair and axon regeneration with functional return of vision. *Proc. Natl. Acad. Sci. U. S. A.* **2006**, *103*, 5054–5059.

[6] Ellis-Behnke, R. G.; Schneider, G. E. Peptide amphiphiles and porous biodegradable scaffolds for tissue regeneration in the brain and spinal cord. *Methods Mol. Biol.* **2011**, *726*, 259–281.

[7] Hartgerink, J. D.; Beniash, E.; Stupp, S. I. Self-assembly and mineralization of peptide-amphiphile nanofibers. *Science* **2001**, *294*, 1684–1688.

[8] Vauthey, S.; Santoso, S.; Gong, H. Y.; Watson, N.; Zhang, S. G. Molecular self-assembly of surfactant-like peptides to form nanotubes and nanovesicles. *Proc. Natl. Acad. Sci. U. S. A.* **2002**, *99*, 5355–5360.

[9] Santoso, S.; Hwang, W.; Hartman, H.; Zhang, S. G. Self-assembly of surfactant-like peptides with variable glycine tails to form nanotubes and nanovesicles. *Nano Lett.* **2002**, *2*, 687–691.

[10] von Maltzahn, G.; Vauthey, S.; Santoso, S.; Zhang, S. G. Positively charged surfactant-like peptides self-assemble into nanostructures. *Langmuir* **2003**, *19*, 4332–4337.

[11] Xu, H.; Wang, Y. M.; Ge, X.; Han, S. Y.; Wang, S. J.; Zhou, P.; Shan, H. H.; Zhao, X. B.; Lu, J. R. Twisted nanotubes formed from ultrashort amphiphilic peptide I_3K and their templating for the fabrication of silica nanotubes. *Chem. Mater.* **2010**, *22*, 5165–5173.

[12] Lakshmanan, A.; Hauser, C. A. E. Ultrasmall peptides self-assemble into diverse nanostructures: Morphological evaluation and potential implications. *Int. J. Mol. Sci.* **2011**, *12*, 5736–5746.

[13] Han, S. Y.; Cao, S. S.; Wang, Y. M.; Wang, J. Q.; Xia, D. H.; Xu, H.; Zhao, X. B.; Lu, J. R. Self-assembly of short peptide amphiphiles: The cooperative effect of hydrophobic interaction and hydrogen bonding. *Chem.-Eur. J.* **2011**, *17*, 13095–13102.

[14] Xu, H.; Wang, J.; Han, S. Y.; Wang, J. Q.; Yu, D. Y.; Zhang, H. Y.; Xia, D. H.; Zhao, X. B.; Waigh, T. A.; Lu, J. R. Hydrophobic-region-induced transitions in self-assembled peptide nanostructures. *Langmuir* **2009**, *25*, 4115–4123.

[15] Pan, F.; Zhao, X. B.; Perumal, S.; Waigh, T. A.; Lu, J. R.; Webster, J. R. P. Interfacial dynamic adsorption and structure of molecular layers of peptide surfactants. *Langmuir* **2009**, *26*, 5690–5696.

[16] Khoe, U.; Yang, Y. L.; Zhang, S. G. Self-assembly of nanodonut structure from a cone-shaped designer lipid-like peptide surfactant. *Langmuir* **2009**, *25*, 4111–4114.

[17] Castelletto, V.; Nutt, D. R.; Hamley, I. W.; Bucak, S.; Cenker, C.; Olsson, U. Structure of single-wall peptide nanotubes: *In situ* flow aligning X-ray diffraction. *Chem. Commun.* **2010**, *46*, 6270–6272.

[18] Hauser, C. A.; Deng, R. S.; Mishra, A.; Loo, Y.; Khoe, U.; Zhuang, F. R.; Cheong, D. W.; Accardo, A.; Sullivan, M. B.; Riekel, C.; et al. Natural tri- to hexapeptides self-assemble in water to amyloid β-type fiber aggregates by unexpected α-helical intermediate structures. *Proc. Natl. Acad. Sci. U. S. A.* **2011**, *108*, 1361–1366.

[19] Wang, J.; Han, S. Y.; Meng, G.; Xu, H.; Xia, D. H.; Zhao, X. B.; Schweins, R.; Lu, J. R. Dynamic self-assembly of surfactant-like peptides A_6K and A_9K. *Soft Matter* **2009**, *5*, 3870–3878.

[20] Baumann, M. K.; Textor, M.; Reimhult, E. Understanding self-assembled amphiphilic peptide supramolecular structures from primary structure helix propensity. *Langmuir* **2008**, *24*, 7645–7647.

[21] Bucak, S.; Cenker, C.; Nasir, I.; Olsson, U.; Zackrisson, M. Peptide nanotube nematic phase. *Langmuir* **2009**, *25*, 4262–4265.

[22] Wang, S. J.; Ge, X.; Xue, J. Y.; Fan, H. M.; Mu, L. J.; Li, Y. P.; Xu, H.; Lu, J. R. Mechanistic processes underlying biomimetic synthesis of silica nanotubes from self-assembled ultrashort peptide templates. *Chem. Mater.* **2011**, *23*, 2466–2474.

[23] Yang, S. J.; Zhang, S. G. Self-assembling behavior of designer lipid-like peptides. *Supramol. Chem.* **2006**, *18*, 389–396.

[24] Pontoni, D.; Finet, S.; Narayanan, T.; Rennie, A. R. Interactions and kinetic arrest in an adhesive hard-sphere colloidal system. *J. Chem. Phys.* **2003**, *119*, 6157–6165.

[25] Schneidman-Duhovny, D.; Hammel, M.; Tainer, J. A.; Sali, A. Accurate SAXS profile computation and its assessment by contrast variation experiments. *Biophys. J.* **2013**, *105*, 962–974.

[26] Schneidman-Duhovny, D.; Hammel, M.; Sali, A. FoXS: A web server for rapid computation and fitting of SAXS profiles. *Nucleic Acids Res.* **2010**, *38*, W540–W544.

[27] Pashuck, E. T.; Cui, H. G.; Stupp, S. I. Tuning supramolecular rigidity of peptide fibers through molecular structure. *J. Am. Chem. Soc.* **2010**, *132*, 6041–6046.

[28] Kawaguchi, T. Radii of gyration and scattering functions of a torus and its derivatives. *J. Appl. Crystallogr.* **2001**, *34*, 580–584.

[29] Selinger, J. V.; Spector, M. S.; Schnur, J. M. Theory of self-assembled tubules and helical ribbons. *J. Phys. Chem. B* **2001**, *105*, 7157–7169.

[30] Teixeira, C. V.; Amenitsch, H.; Fukushima, T.; Hill, J. P.; Jin, W.; Aida, T.; Hotokka, M.; Lindén, M. Form factor of an N-layered helical tape and its application to nanotube formation of hexa-peri-hexabenzocoronene-based molecules. *J. Appl. Crystallogr.* **2010**, *43*, 850–857.

[31] Pringle, O. A.; Schmidt, P. W. Small-angle X-ray scattering from helical macromolecules. *J. Appl. Crystallogr.* **1971**, *4*, 290–293.

[32] Pedersen, J. S. Analysis of small-angle scattering data from colloid and polymer solutions: Modeling and least-square fitting. *Adv. Colloid Interface Sci.* **1997**, *70*, 171–210.

[33] Hamley, I. W. Form factor of helical ribbons. *Macromolecules* **2008**, *41*, 8948–8950.

[34] Rudra, J. S.; Tian, Y. F.; Jung, J. P.; Collier, J. H. A self-assembling peptide acting as an immune adjuvant. *Proc. Natl. Acad. Sci. U. S. A.* **2010**, *107*, 622–627.

[35] Collier, J. H.; Messersmith, P. B. Enzymatic modification of self-assembled peptide structures with tissue transglutaminase. *Bioconjugate Chem.* **2003**, *14*, 748–755.

[36] Hicks, M. R.; Damianoglou, A.; Rodger, A.; Dafforn, T. R. Folding and membrane insertion of the pore-forming peptide gramicidin occur as a concerted process. *J. Mol. Biol.* **2008**, *383*, 358–366.

[37] Chen, C.-L.; Zhang, P. J.; Rosi, N. L. A new peptide-based method for the design and synthesis of nanoparticle super-structures: Construction of highly ordered gold nanoparticle double helices. *J. Am. Chem. Soc.* **2008**, *130*, 13555–13557.

[38] Paramonov, S. E.; Jun, H.-W.; Hartgerink, J. D. Self-assembly of peptide-amphiphile nanofibers: The roles of hydrogen bonding and amphiphilic packing. *J. Am. Chem. Soc.* **2006**, *128*, 7291–7298.

[39] Dong, H.; Paramonov, S. E.; Aulisa, L.; Bakota, E. L.; Hartgerink, J. D. Self-assembly of multidomain peptides: Balancing molecular frustration controls conformation and nanostructure. *J. Am. Chem. Soc.* **2007**, *129*, 12468–12472.

[40] Cenker, Ç. Ç.; Bomans, P. H. H.; Friedrich, H.; Dedeoglu, B.; Aviyente, V.; Olsson, U.; Sommerdijk, N. A. J. M.; Bucak, S. Peptide nanotube formation: A crystal growth process. *Soft Matter* **2012**, *8*, 7463–7470.

[41] Fishwick, C. W. G.; Beevers, A. J.; Carrick, L. M.; Whitehouse, C. D.; Aggeli, A.; Boden, N. Structures of helical β-tapes and twisted ribbons: The role of side-chain interactions on twist and bend behavior. *Nano Lett.* **2003**, *3*, 1475–1479.

[42] Armon, S.; Aharoni, H.; Moshe, M.; Sharon, E. Shape selection in chiral ribbons: From seed pods to supramolecular assemblies. *Soft Matter* **2014**, *10*, 2733–2740.

[43] Cui, H. G.; Webber, M. J.; Stupp, S. I. Self-assembly of peptide amphiphiles: From molecules to nanostructures to biomaterials. *Peptide Sci.* **2010**, *94*, 1–18.

[44] Hamley, I. W. Self-assembly of amphiphilic peptides. *Soft Matter* **2011**, *7,* 4122–4138.

[45] Yao, Y.; Xue, M.; Chen, J. Z.; Zhang, M. M.; Huang, F. H. An amphiphilic pillar[5]arene: Synthesis, controllable self-assembly in water, and application in calcein release and TNT adsorption. *J. Am. Chem. Soc.* **2012**, *134*, 15712–15715.

[46] Yao, Y.; Xue, M.; Zhang, Z. B.; Zhang, M. M.; Wang, Y.; Huang, F. H. Gold nanoparticles stabilized by an amphiphilic pillar[5]arene: Preparation, self-assembly into composite microtubes in water and application in green catalysis. *Chem. Sci.* **2013**, *4*, 3667–3672.

[47] Yu, G. C.; Ma, Y. J.; Han, C. Y.; Yao, Y.; Tang, G. P.; Mao, Z. W.; Gao, C. Y.; Huang, F. H A sugar-functionalized amphiphilic pillar[5]arene: Synthesis, self-assembly in water, and application in bacterial cell agglutination. *J. Am. Chem. Soc.* **2013**, *135*, 10310–10313.

[48] Amenitsch, H.; Rappolt, M.; Kriechbaum, M.; Mio, H.; Laggner, P.; Bernstorff, S. First performance assessment of the small-angle X-ray scattering beamline at ELETTRA. *J. Synchrotron Rad.* **1998**, *5*, 506–508.

[49] European Synchrotron Radiation Facility, Fit2D. http://www.esrf.eu/computing/scientific/FIT2D/ (accessed August, 2014).

[50] Orthaber, D.; Bergmann, A.; Glatter, O. SAXS experiments on absolute scale with Kratky systems using water as a secondary standard. *J. Appl. Crystallogr.* **2000**, *33*, 218–225.

[51] Chung, D. S.; Benedek, G. B.; Konikoff, F. M.; Donovan, J. M. Elastic free energy of anisotropic helical ribbons as metastable intermediates in the crystallization of cholesterol. *Proc. Natl. Acad. Sci. U. S. A.* **1993**, *90*, 11341–11345.

[52] Lees, J. G.; Smith, B. R.; Wien, F.; Miles, A. J.; Wallace, B. A. CDtool—An integrated software package for circular dichroism spectroscopic data processing, analysis, and archiving. *Anal. Biochem.* **2004**, *332*, 285–289.

[53] Blender Foundation. http://www.blender.org/ (accessed August, 2014).